CEAS-GNC-2022-011

CEAS EuroGNC 2022
"Conference on Guidance, Navigation and Control"
3-5 May 2022 @ Technische Universität Berlin, Germany

Asymmetric Stall Modeling of the Cessna Citation II Aircraft

A. Delfosse MSc student, Delft University of Technology, Control and Simulation, 2629HS, Delft, the Netherlands. a.delfosse@student.tudelft.nl

C.C. de Visser Associate Professor, Delft University of Technology, Control and Simulation, 2629HS, Delft, the Netherlands. c.c.devisser@tudelft.nl

D.M. Pool Assistant Professor, Delft University of Technology, Control and Simulation, 2629HS, Delft, the Netherlands. d.m.pool@tudelft.nl

ABSTRACT

As of 2019, the FAA and EASA require all airline pilots to complete stall and recovery training as integral part of their training. To mitigate risks, this training takes place in ground-based simulators. To enable this, realistic models of aircraft behaviour in the stall regime need to be developed. In this paper, a new aerodynamic stall modelling methodology is proposed that combines classical aerodynamic model identification techniques with a novel adaptation of Kirchhoffs theory of flow separation that considers flow separation over both wings separately. This new model is called the 2X model, as it contains 2 independent flow separation variables, i.e. one for each wing. The model parameters are estimated based on flight experiments in the stall regime conducted with a Cessna Citation II laboratory aircraft operated by the TU-Delft. The developed model for the first time allows accurate prediction of lateral-directional dynamics encountered during stall such as e.g. wing-dip. In addition, it was found that the 2X model also improved predictions of longitudinal stall dynamics leading to a new extended envelope aerodynamic model for the Cessna Citation II that now also includes stall entry and post-stall aerodynamics.

1 Nomenclature

a_1	=	Stall abruptness parameter
c	=	chord
C_D	=	Drag coefficient
C_L	=	Lift coefficient
C_l	=	Rolling moment coefficient
C_n	=	Yawing moment coefficient
C_T	=	Thrust coefficient
C_Y	=	Side force coefficient
C_{α_0}	=	Vane geometric coefficient coefficient
$C_{\alpha_{up}}$	=	vane upwash coefficient
J	=	Cost function
M	=	Mach number
p	=	Roll rate

q = Pitch rate
r = Yaw rate
$X_{L,R}$ = Flow separation point locations
α = Angle of attack
* = Stall angle of attack
β = Angle of sideslip
δ_a = Aileron deflection
δ_e = Elevator deflection
δ_e = Rudder deflection
τ_1 = Time delay due to flow inertia
τ_2 = Flow hysteresis effect
t = time step

2 Introduction

Currently, LOC-I (Loss Of Control In flight) remains the primary cause of aviation fatalities [1] . In this context, aircraft stall prevention and stall recovery training could be a game changer for the safety of the commercial aircraft.
Similarly to the FAA which requires US airline pilots to follow stall training since March 2019 [2], from April 2019 the EASA requires European airline pilots to follow stall training, referred to as 'Upset Prevention and Recovery Training' (UPRT) [3]. For obvious cost and safety considerations, training pilots in actual aircraft is not considered a viable option. Hence, this training taking place in full motion flight simulators.

For this reason, significant research and development efforts have been made towards the extension of the conventional nominal flight envelope that can be simulated to also include stall onset, stall, and post-stall dynamics in flight simulation training devices (FSTDs). This extension of the aerodynamic flight envelope has the goal to provide pilots positive transfer of training in case of upset and stall conditions in order to help them acquire skills to recognize, prevent and recover from such conditions in a safe manner. Unlike for the nominal flight envelope, at high angles of attack close to and beyond the stall, the aerodynamics can present a highly non-linear, unsteady, configuration-dependent, and fundamentally unpredictable (chaotic) behaviour. This makes the task of creating and implementing a high fidelity stall models challenging, and encourages the use of new original and innovative data gathering and modeling techniques, with standard stationary methods no longer being viable. One of the possible ways of modeling stall is using Kirchhoff's theory of flow separation in the aerodynamic model identification process [4] [5] [6] [7] [8]. This allows one to capture and model non-linearities such as alpha-hysteresis by introducing into the aerodynamic model an internal flow separation variable X, that can be estimated by (iteratively) solving an ordinary differential equation within the parameter estimation process [4]. This technique proved to be effective in modelling in particular the low-frequency longitudinal dynamics during a stall. Nevertheless, there are still blindspots concerning the development of a full envelope high fidelity stall model. Especially the lateral-directional dynamics cannot be captured using the standard Kirchhoff based approach since it assumes flow separation to be a symmetric phenomena [9]. However, because stalls are often accompanied by significant lateral-directional dynamics and divergence such as sudden asymmetric wing drop, lateral-directional stall dynamics should be included the simulator stall models to make an effective training device.

Hence, the main contribution of this work is to close this gap and implement the necessary tools for lateral-directional stall dynamics modeling using flight test data by means of an extension of the classical Kirchhoff flow separation theory from one global flow separation variable to two wing-specific separation variables, in a new approach we call the 2X approach. Using two flow separation variables instead of

one by itself is not new, see [9]. The novelty of the present work is: 1) we do not neglect transient effects (modelled by the τ_1 variable); 2) we include an automated (stall) model structure selection procedure based on multivariate orthogonal functions (MOF) for all of the force and moment coefficients in clean and landing configurations; 3) We apply this methodology to flight data obtained in the stall domain during which the aircraft was excited with specific system identification inputs.

3 Flight Test Data

Enjoying the immense advantage of co-owning (with NLR [10]) a Cessna Citation II aircraft (registered as PH-LAB) equipped with a dedicated flight test instrumentation system (FTIS) which records data from many sensors (as described in table 3), the Delft University of technology Citation Stall Modeling task force has at its disposal a state-of-the-art laboratory for conducting flight tests in the stall and post-stall flight regions.

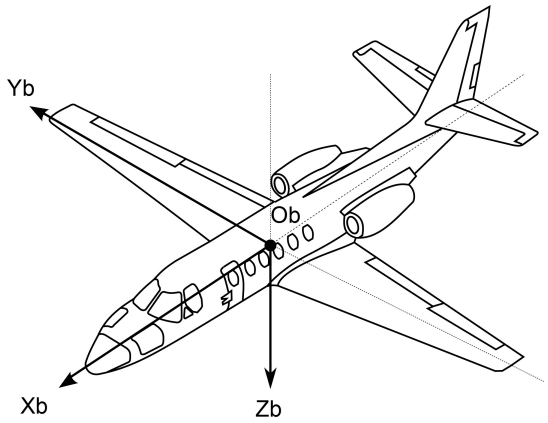

Fig. 1 Schematic view of the Cessna Citation II, including the air data boom.

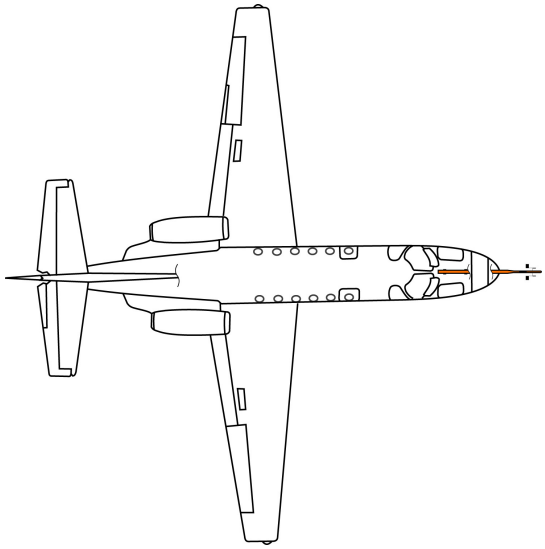

Fig. 2 Schematic view of the Cessna Citation II with the body-fixed reference frame axes definition.

Table 1 Citation II Dimensions

Dimensions	
length	$14.4m$
b	$15.9m$
b_{tail}	$5.8m$
$\bar{c}$	$2.09m$
S	$30m^2$
S_{tail}	$6.2m^2$

Table 2 Citation II Dimensions, Mass & Inertia

Mass & Inertia	
MTOW	$6,600kg$
MLW	$6,100kg$
Dry mass	$4,157kg$
Ixx	$12,392kg.m^2$
Iyy	$31,501kg.m^2$
Izz	$41,908kg.m^2$
Ixz	$2,252.2kg.m^2$

The Cessna Citation II is a small twin-engine business jet aircraft with unswept tapered wings (taper ratio of 0.316) accompanied by a small amount of dihedral of about 4.5° and an aspect ratio of 7.8.

Flight experiments have been conducted in two different aircraft configurations: a clean configuration and a landing configuration with flaps and landing gear extended. Different control surface excitation schemes were used to obtain informative data: 3-2-1-1 and aileron frequency sweeps, also known as

Equipment	Description	Measures	Units	Variables
GPS	High accuracy global positioning system (using phase tracking)	Position in FE	m	x_E, y_E, z_E
		Velocity in FE	m/s	$\dot{x_E}$, $\dot{y_E}$, $\dot{z_E}$
DADC	Digital airdata computer	Total airspeed	m/s	V_{TAS}
AHRS	Attitude and heading reference system (inertial reference system)	Aircraft attitude	rad	ϕ, θ, ψ
		Body rotation rates	rad/s	p, q, r
		Body specific forces	m/s2	A_x, A_y, A_z
Synchros	Angle measurements	Control surf. defl.	rad	δ_a, δ_e, δ_r
Boom	Air data boom	Air incidence angle	rad	α, β

Table 3 Citation II flight test equipment and measured variables, which are relevant to the research

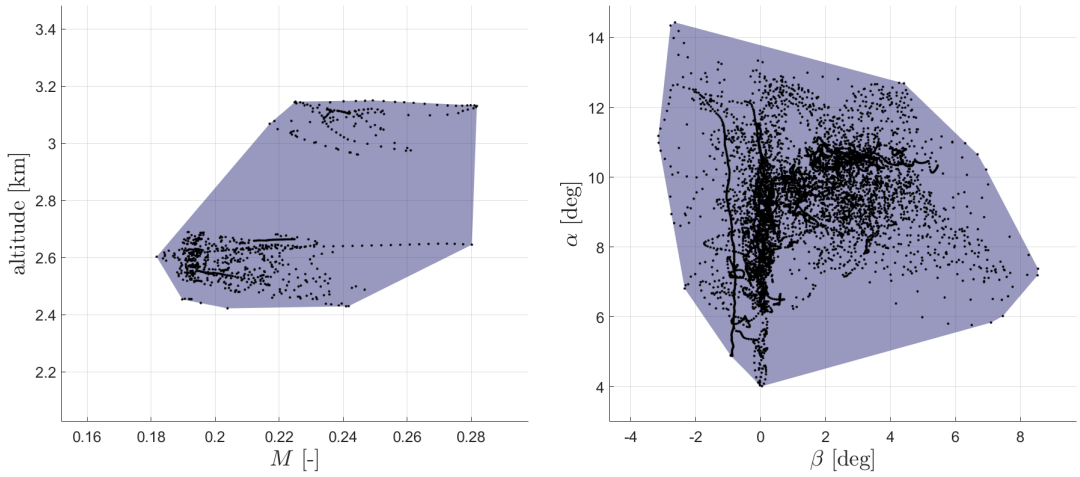

Fig. 3 Clean Configuration Flight Envelope

'aileron wiggle'. The 3-2-1-1 can be performed either by excitation of a unique control surface (elevator, ailerons, rudder), or simultaneously on two (elevator + ailerons, elevator + rudder, ailerons + rudder) or even the three control surfaces (elevator + ailerons + rudder). These manoeuvres were flown while the aircraft was entering a stall, while the aircraft was in the stall, and during stall recovery [11] [12] [13].

The data were gathered around $2600/3200m$ altitude for the clean configuration (with 46 data sets in total, split so that 36 are used for training purpose and 10 for validation purpose) as shown in figure 3; and mainly around $3200m$ altitude for the landing configuration (with 22 data sets in total, split so that 16 are used for training purpose and 6 for validation purpose) as shown in figure 4.
The data are accompanied by a flight test logbook which allows detailed monitoring of the aircraft manoeuvre execution (input used, altitude, flight conditions, aircraft response, etc.).

	Clean Config	Landing Config
Training Data Sets	36	16
Validation Data Sets	10	6

Before running the flight path reconstruction and the model identification procedures, the data were pre-processed by low-pass filtering them using a Butterworth filter of order 4 through MATLAB's function $filtfilt$. Indeed, the states resulting from numerical differentiation (for instance $\dot{\alpha}$, $\dot{\beta}$, $\dot{p}$, $\dot{q}$, $\dot{r}$, etc) need filtering due to amplified signal noise. Additionally, since we are interested in the low-frequency,

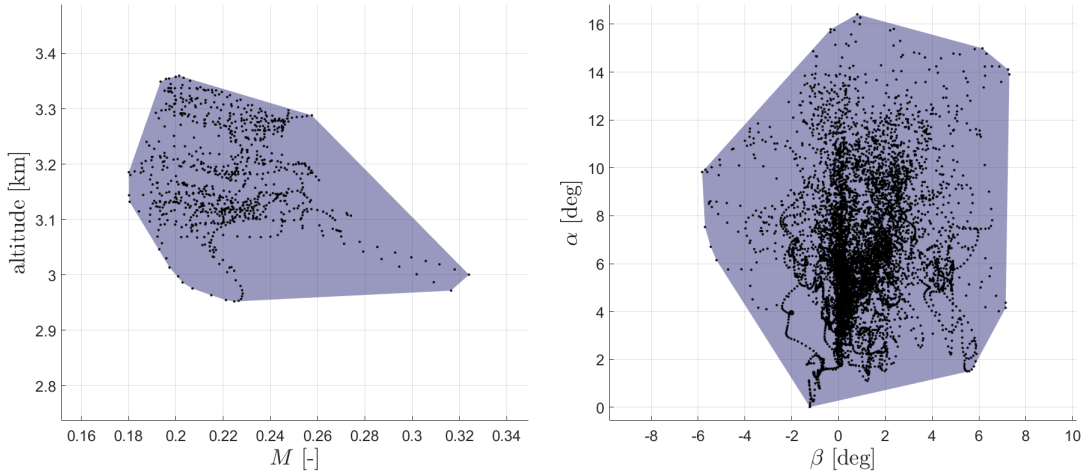

Fig. 4 Landing Configuration Flight Envelope

high-amplitude dynamics of stall, another main noise sources that needs to be filtered are the vibrations due to the stall buffet. Even if buffet vibrations are essential to build a realistic stall simulation model, as the buffet provides pilots with essential information about an imminent stall [7] , for the purpose of this research these have been filtered out. Note that the high frequency stall buffet model is built in parallel using the same flight data but using frequency domain methods that are better suited for capturing oscillatory behavior [7][14]. Eventually, the complete stall model to be used in the simulator consists of the summation of the low-frequency model that captures the high amplitude motions and a stall buffet model that captures the high-frequency oscillatory behavior.

4 Stall Model Structure Selection and Parameter Estimation

The Kirchhoff theory of flow separation has been developed in order to essentially model longitudinal non-linear effects happening during stalls. Nevertheless, with some manipulations and adaptations it is possible to exploit Kirchhoff theory of flow separation to model asymmetrical effects.
The new idea here is based on the fact that lateral-directional effects during stalls are due (at least in part) to the fact that flow separation does not happen at the same time / same point on the left wing and on the right wing.
The flow separation point location being governed by the angle of attack of the wing relative to the airstream, the first step in this process is to determine the local angles of attack of both left and right wings. Then an asymmetric stall model can be proposed according to the asymmetric flow separation profile.

4.1 Local Airflow Angles Determination

In order to obtain the per-wing angle of attack without having dedicated angle of attack sensors for both wings, we use the approach presented in [15]. The velocity at any arbitrary point P on a rigid-body aircraft flying in a non-moving atmosphere can be written as follows:

$$\overrightarrow{V_P} = \overrightarrow{V_{cg}} + \overrightarrow{\omega} \times \overrightarrow{r_P} \tag{1}$$

Or in matrix form :

$$\begin{bmatrix} u_P \\ v_P \\ w_P \end{bmatrix} = \begin{bmatrix} u_{cg} \\ v_{cg} \\ w_{cg} \end{bmatrix} + \begin{bmatrix} 0 & -r & q \\ r & 0 & -p \\ -q & p & 0 \end{bmatrix} \begin{bmatrix} x_P \\ y_P \\ z_P \end{bmatrix} \tag{2}$$

It is thus possible to express the flow angles at any point of the wings, depending on the flow components velocity at the c.g., angular rates of the aircraft and the location - relatively to the c.g. - at which the new flow angles have to be expressed. This is done first by computing the new flow velocities components and then, by using the classical flight dynamics formulas for flow angles.

$$\alpha_P = \arctan \frac{w_P}{u_P} = \arctan \frac{w_{cg} - q.x_P + p.y_P}{u_{cg} - r.y_P + q.z_P} \tag{3}$$

$$\beta_P = \arcsin \frac{u_P}{V_P} = \arctan \tan \mu \cos \alpha \tag{4}$$

$$\mu_P = \arctan \frac{v_P}{u_P} = \arctan \frac{v_{cg} + r.x_P - p.z_P}{u_{cg} - r.y_P + q.z_P} \tag{5}$$

These equations are useful because they allow using only one measurement of airspeed to determine the value of the airspeed at any point on the wings and subsequently the local angles of attack at any points on the wings.

Additionally, it is possible to pass easily from the flow angles to the airspeed components (flow angles and total airspeed being the variables recorded in flight), using the formulas :

•V, α, $\mu \rightarrow u, v, w$

$$\begin{cases} u = \frac{V}{\sqrt{1+tan^2(\alpha)+tan^2(\mu)}} \\ v = \frac{V.tan(\mu)}{\sqrt{1+tan^2(\alpha)+tan^2(\mu)}} \\ w = \frac{V.tan(\alpha)}{\sqrt{1+tan^2(\alpha)+tan^2(\mu)}} \end{cases} \tag{6}$$

•V, α, $\beta \rightarrow u, v, w$

$$\begin{cases} u = V.cos(\alpha).cos(\beta) \\ v = V.sin(\beta) \\ w = V.sin(\alpha).sin(\beta) \end{cases} \tag{7}$$

This yields a convenient method for the determination of the local angle of attack on left and right wings, separately. It is then possible to determine the flow separation points on each wings according to the local AOA and later estimate and model the induced asymmetrical aerodynamic effects. In this work a new '2X' model is proposed in which two separate flow separation point location will be considered : one for the left and one for the right wing.

4.2 Kirchhoff Theory of Flow Separation for Asymmetrical Flows

The purpose of this research is to evaluate the applicability of two independent flow separation points (one located on each wing) in the model instead of just one, in particular in terms of asymmetrical variable modeling (lateral-directional motion).

The classical Kirchhoff ODE governing the position of the flow separation point [4] is used, but in our case the angle of attack and the angle of attack rate used are the local ones (α_L, α_R and $\dot{\alpha_L}$, $\dot{\alpha_R}$) which are computed from the data recorded during the flight test using the formulas described in section 4.1. Here we use $x_p = 0$ and $z_p = 0$, but to obtain the local angles of attack at each wing two values of y_p

have been used ($y_p = -\frac{b}{2}$ for the left wing and $y_p = +\frac{b}{2}$ for the right wing).

$$\tau_1 \frac{dX_{L,R}}{dt} + X_{L,R} = X_{0_{L,R}}(\alpha_{L,R} - \tau_2 \dot{\alpha_{L,R}}) \tag{8}$$

With separate α_L and α_R for the new 2X model and $\alpha_L = \alpha_R = \alpha$ for the standard 1X model. This function depends on four parameters that needs to be estimated using the experimental data.

- a_1 is a shape parameter which is linked to the abruptness of the stall - more this value is high, more the stall will be abrupt.
- α^* is the angle of attack where $X = \frac{1}{2}$ which can also be called the stall angle of attack.
- τ_1 represents the transient effects of the flow separation point - the time needed to readjust to the new flow conditions when these changes.
- τ_2 which account for the hysteresis effect - dependency of the flow separation point location on the angle of attack rate $\dot{\alpha}$.

These parameters are considered to be identical for both wings. The logic behind it is that both wings are considered to be identical (they are symmetric), hence their aerodynamic behaviour and the parameters governing it should also be identical. This also avoids having unnecessary many model terms to estimate while also preventing correlations between parameters to negatively impact numerical conditioning of the estimator.

The modelling results of the new 2X model will be presented along with the result of the previous standard 1X model as comparison material in order to determine and evaluate the possible benefits of this new model.

For the 2X case, 2 different variants will first be considered, before being reduced to a final variant.

In order to solve Kirchhoff's ODE and obtain the X-parameters, a model for the lift coefficient first needs to be defined. For the 1X model, the lift formulation considered is the classic one, as expressed by equation 9

$$C_L = C_{L_0} + C_{L_\alpha} \left\{ \frac{1 + \sqrt{X}}{2} \right\}^2 \alpha + C_{L_{\bar{q}}} \bar{q} + C_{L_{\delta_e}} \delta_e \tag{9}$$

For the 2X model, the lift formulation assumes split contributions to the local wings angle of attack, as shown in equation 10

$$C_L = C_{L_0} + C_{L_{\alpha_L}} \left(\frac{1 + \sqrt{X_L}}{2} \right)^2 \alpha_L + C_{L_{\alpha_R}} \left(\frac{1 + \sqrt{X_R}}{2} \right)^2 \alpha_R + C_{L_{\bar{q}}} \bar{q} + C_{L_{\delta_e}} \delta_e \tag{10}$$

The last considered formulation for the lift coefficient also used in the 2X approach considers only one $C_{L_\alpha} = C_{L_{\alpha_L}} = C_{L_{\alpha_R}}$. This is done taking into consideration the symmetrical profile of the left and right wings just as it is done previously in Kirchhoff ODE to consider the set of X parameters obtained (τ_1, τ_2, a_1, α^*) unique and not proper to each wing. Hence, the lift model obtained is described by equation 11 :

$$C_L = C_{L_0} + C_{L_{\alpha_L}} \left[\left(\frac{1 + \sqrt{X_L}}{2} \right)^2 \alpha_L + \left(\frac{1 + \sqrt{X_R}}{2} \right)^2 \alpha_R \right] + C_{L_{\bar{q}}} \bar{q} + C_{L_{\delta_e}} \delta_e \tag{11}$$

4.3 Parameter estimation

A non linear optimization technique is required to identify the set of X parameters (τ_1, τ_2, a_1, α^*) by solving Kirchhoff's ODE for the two considered flow separation points (X_L and X_R) supplying the local angle of attack (α_L and α_R computed using the equations that can be found in the section 4.1 for the tip of each wing) and local angle of attack rate ($\dot{\alpha_L}$ and $\dot{\alpha_R}$, obtained by numerical differentiation of α_L and α_R) for respectively the left and right wings. The nonlinear optimization is performed using the $fmincon$ function in Matlab, using many semi-random initial conditions for the parameters in order to reduce the chances of ending up in a local optimum. The cost function is a classical mean squared error (MSE) of the lift coefficient.

The optimization procedure is conducted by minimising the error between the measured and modelled lift coefficient C_L, considering the relationship between X and C_L - described in equations 9 11 10.

The nonlinear optimization problem will yield an estimate of both the parameters of the aerodynamic lift coefficient model C_{L_i}, as well as the 4 parameters of Kirchhoff's ODE (τ_1, τ_2, a_1, α^*). An initial model structure of the lift coefficient C_L with initial values of the parameters is needed. These are described in equations 9 11 10. The model structure of the lift coefficient C_L can then be improved iteratively by solving for the X-parameters using the nonlinear optimization problem and then running the model term selection algorithm to improve the C_L model structure if needed, and eventually re-run the non linear optimization process if any changes have been made in the C_L model.

4.4 Model Structure Selection & Multivariate Orthogonal Function modelling

Obtaining an adequate model structure for the 1X and 2X models is not trivial as they may contain both classical model terms as well as model terms containing the flow separation point(s). In this work, an automated procedure is developed that is based on the work done by Morelli et al [16]. The multivariate orthogonal function (MOF) modelling technique is used to determine global aerodynamic models structures by selecting candidate terms from a pool of candidates. Each term is made mutually orthogonal in order to decouple them which allows them to be individually assessed for their contribution to the model fit.

$$y = \sum_{j=1}^{n} a_j.p_j + \epsilon = P.a + \epsilon \tag{12}$$

A multivariate orthogonal function is formed by a linear combination of the multivariate orthogonal model terms p_j and their parameters a_j as described by equation 12. Here P is the vector composed of the individual model terms p_j and a the vector containing the corresponding model parameters a_j.

To obtain the highest quality model, the goal is to minimize the model error ϵ. This is done through the use of a cost function that estimates the model parameters a_j so ϵ is minimized. The cost function is once again a least squares function, described by equation 13

$$J = \frac{1}{2}\epsilon^T\epsilon = \frac{1}{2}(y - P.a)^T(y - P.a) \tag{13}$$

The model terms are supposed to be orthogonal, as described by equation 14, so the cost function can be developed and simplified to be re-written as in equation 15.

$$\text{for i,j} = 1, ...,\text{n } \& \; i \neq j, p_i p_j = 0 \tag{14}$$

$$J = \frac{1}{2}\left[y^T.y - \sum_{j=1}^{n} \frac{(p_j.y)^2}{p_j^T.p_j} \right] \tag{15}$$

The model parameters to be estimated depend exclusively on their corresponding model term p_j and the measurement vector y :

$$\hat{a_j} = \frac{p_j.y}{p_j^T.p_j} \tag{16}$$

The candidate contributions are quantified based on the effect that they would have on the predicted square error (PSE), as in equation 17. This is constituted of two contributions : the model fit error (MSE) plus a model complexity penalty term. It quantifies the improvement in cost function J minimisation while simultaneously penalising the addition of the model term that increases the model complexity.

$$PSE = \frac{(y - P.\hat{a})^T(y - P.\hat{a})}{N} + \sigma_y^2 \frac{n}{N} = \frac{2.\hat{J}}{N} + \sigma_y^2 \frac{n}{N} \tag{17}$$

With N the number of data points, n the current number of terms used in the model, and σ_y^2 the variance of the modeled signal y (that can be expressed by equation 18), which is used as a scaling term.

$$\sigma_y^2 = \frac{1}{N-1} sum_{i=1}^{N} (y_i - \bar{y_i}) \tag{18}$$

With $\bar{y_i} = \frac{1}{N}\sum_{i=1}^{N} z_i$

The modification in PSE due to the addition of a candidate term j is given by equation 19

$$\Delta PSE_j = -\frac{(p_j^T.y)^2}{p_j^T.p_j} + \frac{1}{N}\sigma_y^2 \tag{19}$$

Adding model terms to the cost function will on the one hand improve the model fit and thus decrease the value of the cost function, but on the other will increase model complexity and thus increase the value of the penalty of the PSE. If the model terms are added in the correct order (from the most effective to the least effective modelling term), at some point the increased model complexity penalty will out weight the decrease in cost function due to improved model fit. At this moment, a global minimum has been reached by the PSE, and the global model structure should be kept as it is at this step.

5 Results

The identification of an aerodynamic model of the Cessna Citation II aircraft including asymmetric dynamics has been conducted for clean configuration and landing configuration (with flaps and landing gear extended). The split of the data set for either training or validation purpose was made on a random basis, with a ratio of 80%/20% for the clean configuration and 70%/30% for the landing configuration (which count less data set).

First, the results of the nonlinear X-parameter optimization for the different models will be presented. Then, the model structure selections results for each of the aerodynamic coefficients of interest are presented and analysed.

5.1 Kirchhoff ODE & Lift Coefficient parameters analysis

As a reminder, 3 'initial' Lift Coefficient C_L models - which are needed to solve the non linear optimization problem that gives the X parameters - have been considered and evaluated. These are The '1X Model' in equation 9, the '2X $2C_{L_\alpha}$ Model' in equation 10, and the '2X $1C_{L_\alpha}$ Model' in equation 11.

5.1.1 X parameter analysis

The results are found to be coherent with previous work [7] [6] and are well distributed without clusters near a bound - which can happen if the selected bounds are not well suited for the optimization problem.

	1X $1C_{L_\alpha}$		2X $1C_{L_\alpha}$		2X $2C_{L_\alpha}$	
	$\hat{\theta}$	var	$\hat{\theta}$	var	$\hat{\theta}$	var
τ_1	0.4903	0.0679	0.5590	0.0702	0.4087	0.0362
τ_2	0.1538	0.01334	0.2503	0.0171	0.2179	0.0065
a_1	33.3673	32.0890	30.6863	68.2578	26.9272	27.9854
α^*	0.2425	0.0008	0.2394	0.0031	0.2474	0.0007

Table 4 Obtained X parameters for the different models in clean configuration

The sets of X-parameters, obtained for the different Lift models, presented in Table 4 for the clean configuration and Table 5 for the landing configuration are all quite similar. In terms of mean values, variances, but also dispersion, they present results that are close to each other. More details about the distribution and the correlation between the parameters for the different models can be found the appendices.

Even if a small discrepancy is observable for the different models, and in particular for the τ_2 parameter, a look at the time-domain influence of a variation of these parameters figure 5 - within the range of figures obtained here - confirms that the sensitivity of the Lift Coefficient C_L to such variations is low. The parameters which have the most significant influence are the static parameters : a_1 and

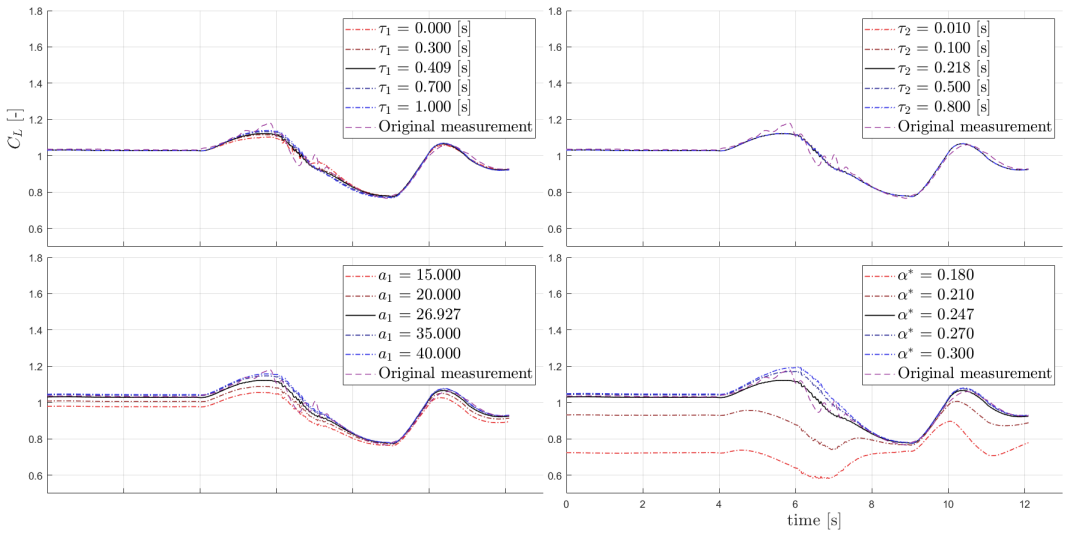

Fig. 5 C_L sensitivity to X-parameters modification, Clean configuration, 2X $2C_{L_\alpha}$ Model based on flight data

even more so the stall angle of attack α^*. Concerning the dynamic parameter τ_2 representing the flow

hysteresis, an adequate estimate can be obtained thanks to the highly dynamical stall data used here compared to the previous use of quasi-static stall yielding τ_2 values tending towards 0 [6].

	$1X\ 1C_{L\alpha}$		$2X\ 1C_{L\alpha}$		$2X\ 2C_{L\alpha}$	
	$\hat{\theta}$	var	$\hat{\theta}$	var	$\hat{\theta}$	var
τ_1	0.3532	0.0585	0.3094	0.0668	0.4472	0.0596
τ_2	0.0660	0.0053	0.1083	0.0099	0.1143	0.0135
a_1	33.3021	9.2212	35.7050	19.3535	35.6405	34.1304
α^*	0.1997	0.0018	0.2017	0.0017	0.1851	0.0014

Table 5 Obtained X parameters for the different models in landing configuration

For the landing configuration it is interesting to note that the value of $\alpha^*_{landing}$ is, as expected, inferior to α^*_{clean}. Indeed, this is caused by an up-left shift of the lift curve when the flaps are extended. The other parameters remain in ranges such that their visual influence are very low.

Among these 3 possible models for computing the X parameters, the 2X $2C_{L_\alpha}$ appears to give the best results in term of estimation accuracy and the lowest parameter variance. It greatly improves the accuracy of estimation of the dynamic X parameters (τ_1, τ_2) (at least divides by two the obtained variance) and is about as precise when it comes to computing the static parameters (a_1, α^*). The model formulation combined with the high dynamical content of the flight test data used allowed accurate determination of the X parameters.

5.1.2 Lift Coefficient C_L model parameter analysis

The purpose of this section is to compare the accuracy and efficiency of the different proposed models considered ($1X1C_{L_\alpha}$, $2X2C_{L_\alpha}$, $2X1C_{L_\alpha}$ and the 'blended model' $2X2C_{L_\alpha}$ converted to $2X1C_{L_\alpha}$) for the symmetric dynamics to start with, and to evaluate eventual improvements from one model to another and determine which of the two $2X$ models provides the highest performance. ***•Clean configuration***

Starting from the analysis of the '2X $2C_{L_\alpha}$' model, what can be observed is that all the parameters are normally distributed and present relatively low values of correlation (always inferior to 0.6) as it can be seen in figure 6 ; even for the two C_{L_α} parameters. What is clearly noticeable, is that the values of $C_{L_{\alpha_L}}$ and $C_{L_{\alpha_R}}$ are very close together (at roughly 4% difference), which is logical, considering both right and left wings are symmetric and thus should present similar aerodynamic characteristics.

The Figure 6 represents the distribution of the estimated individual lift coefficient parameters contributions plus their correlation with respect to each of the individual parameters. It can also be used to check the relevance of the chosen parameters, by checking the dispersion of the scatter plot. And finally, it allows for the spotting of outliers, and analyse the reason for their presence (e.g. the data set does not contain adequate excitation of the required dynamics).

	$1X\ 1C_{L\alpha}$		$2X\ 1C_{L\alpha}$		$2X\ 2C_{L\alpha}$ converted to $1C_{L\alpha}$	
	$\hat{\theta}$	var	$\hat{\theta}$	var	$\hat{\theta}$	var
C_{L_0}	0.0893	0.01333	0.0673	0.0221	0.0962	0.0177
C_{L_α}	5.1973	0.4813	2.7430	0.2997	2.5953	0.1652
$C_{L_{\delta_e}}$	0.2414	0.2372	0.0879	0.4422	0.3261	0.2141
C_{L_q}	10.3505	103.9959	8.8671	126.2863	13.8587	65.3707

Table 6 Obtained C_L parameters for the different models (which include a unique C_{L_α}) in clean configuration

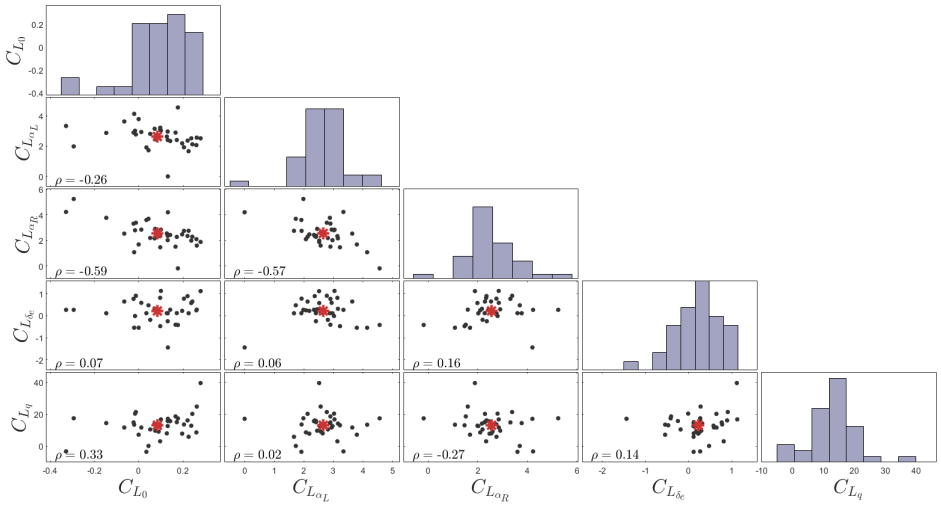

Fig. 6 C_L parameters dispersion and correlation for the 2X and 2 C_{L_α} model

	$\hat{\theta}$	var
C_{L_0}	0.0856	0.0200
$C_{L_{\alpha_L}}$	2.6548	0.6211
$C_{L_{\alpha_R}}$	2.5516	0.9646
$C_{L_{\delta_e}}$	0.2252	0.2833
C_{L_q}	13.1085	61.8766

Table 7 Obtained C_L parameters for the '$2X\ 2C_{L_\alpha}$' model in clean configuration

Considering the time taken to solve for the X parameters of the '2X $1C_{L_\alpha}$' model, which is the longest of the 3 possible model structures, the uniqueness of the C_{L_α} coefficient is interpreted as an additional constraint for the solver which further increases the computational complexity of the optimization. Moreover, it was observed that it was possible to compute an accurate unique C_{L_α} parameter from the $2C_{L_\alpha}$ model, by averaging the value of $C_{L_{\alpha_L}}$ and $C_{L_{\alpha_R}}$, that are relatively close as can be seen in table 7. This method seems to be a better and more efficient alternative which is less time consuming, globally more accurate (reduce variance of almost all parameters, reduces MSE, increases VAF), and gives very close results to the constrained '2X $1C_{L_\alpha}$' model as concluded in table 6.
In appendix 6.2 the distribution and correlation of the C_L parameters for the other - '2X $1C_{L_\alpha}$' and '1X' - models are presented.

The conversion of the '2X $2C_{L_\alpha}$' model to a '2X $1C_{L_\alpha}$' globally yields the best results in terms of variances, and the retained value for the mean C_{L_α} is also close to the one found by the optimisation run with the unique C_{L_α} model (less than 6% difference). Additionally, this value is extremely close to half the value of the C_{L_α} from the 1X model (less than 0.5% of difference).

Finally, by converting the '2X $2C_{L_\alpha}$' model to the '2X $1C_{L_\alpha}$' model, a great model simplification is made without significant costs in terms of accuracy. The model accuracy of the simplest 'old' 1X model is already very accurate with a low MSE, a high VAF and a relatively high R2 coefficient. The new models introducing two distinct flow separation point are as accurate as the classical 1X model at a significance level of less than 1%.

The VAF of all of the data set are above 99%, be it training or validation data. For all the models considered. This means that the CL model is already, in each of its forms, capturing the vast majority of the dynamics.

		$1X$	$2X\ 2C_{L_\alpha}$	$2X\ 1C_{L_\alpha}$ from $2C_{L_\alpha}$
Training	MSE	0.0030	0.0031	0.0031
	R2	0.70	0.69	0.69
	VAF (%)	99.67	99.65	99.66
Validation	MSE	0.0029	0.0044	0.0044
	R2	0.74	0.60	0.60
	VAF (%)	99.67	99.52	99.51

Table 8 Training and Validation results

The final lift model C_L defined as by equation 11 with the corresponding terms coefficient issued from 6 ('2X $1C_{L_\alpha}$' issued from 2X $2C_{L_\alpha}$ model terms) depict nicely the time evolution of the measured lift coefficient during the whole manoeuvre (pre-stall, stall and recovery) and this regardless of the control surface input, as it can bee seen in figure 7 and figure 8.

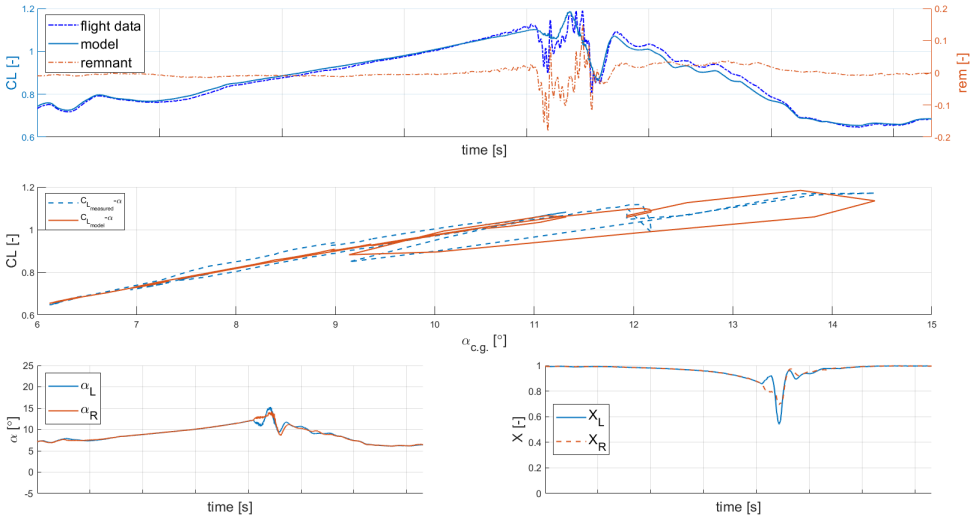

Fig. 7 Example of modeled lift coefficient C_L for the aircraft in clean configuration, during a '3-2-1-1' aileron manoeuvre during the stall

•Landing configuration

	$1X\ 1C_{L\alpha}$		$2X\ 1C_{L\alpha}$		$2X\ 2C_{L\alpha}$ converted to $1C_{L\alpha}$	
	$\hat{\theta}$	var	$\hat{\theta}$	var	$\hat{\theta}$	var
C_{L_0}	0.3978	0.0088	0.4016	0.0081	0.4375	0.0133
C_{L_α}	2.7027	0.6755	1.3476	0.1461	1.6728	0.4113
$C_{L_{\delta_e}}$	-2.9992	0.6079	-2.9204	0.5591	-2.1322	2.6118
C_{L_q}	32.2693	271.1357	34.2620	220.7462	30.3496	207.1190

Table 9 Obtained C_L parameters for the different models in landing configuration

For the landing configuration, the same type of observation can be made as for the clean configuration, except that there is more asymmetry in the estimation of the $C_{L_{\alpha_{L,R}}}$ parameters for '2X $2C_{L_\alpha}$' as shown by Table 10. Nevertheless, when further analysed, it is found that $C_{L_{\alpha_L}}$ and $C_{L_{\alpha_R}}$ are correlated ($\rho = 0.72$) so they likely describe (at least partly) the same dynamic. Considering the remarks previously made for

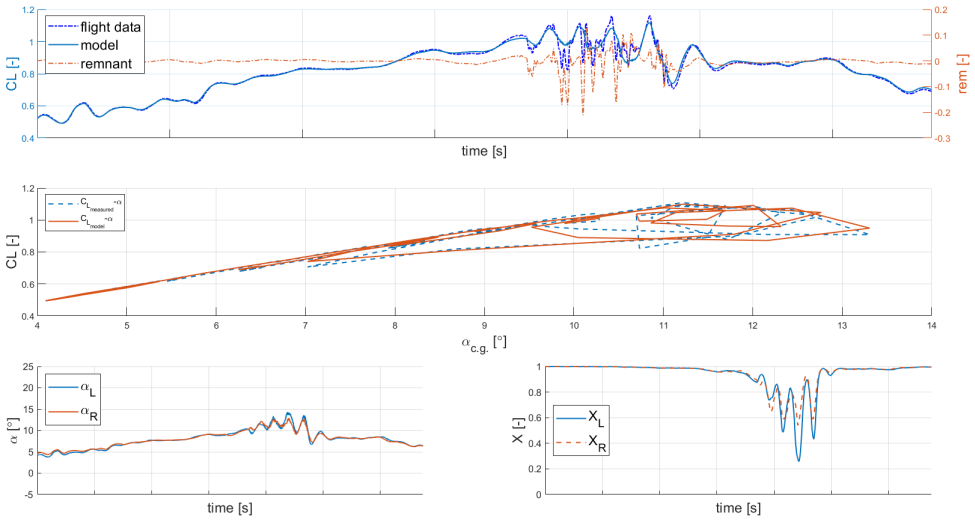

Fig. 8 Example of modeled lift coefficient C_L for the aircraft in clean configuration, during an aileron frequency sweep (AKA 'wiggle') manoeuvre during the stall

	$\hat{\theta}$	var
C_{L_0}	0.3885	0.0087
$C_{L_{\alpha_L}}$	0.9070	1.2130
$C_{L_{\alpha_R}}$	1.8802	1.1930
$C_{L_{\delta_e}}$	-2.9980	0.5136
C_{L_q}	33.2396	232.2020

Table 10 Obtained C_L parameters for the '$2X\ 2C_{L_\alpha}$' model in landing configuration

the clean configuration model and the obtained results, it has been determined that also here the '2X $2C_{L_\alpha}$' can be converted to a '2X $1C_{L_\alpha}$' to simplify the model structure and optimize computation time without significantly degrading the final model accuracy.

One can remark that for the landing configuration the average C_L is higher than for the clean configuration, in accordance to the deployment of flaps, to increase lift (which also increases drag and lowers the stall angle of attack). Another remark that can be made for the landing configuration is that, as expected, the bias in the lift coefficient $C_{L_{0_{landing}}}$ is higher than the bias in the lift coefficient in clean conditions $C_{L_{0_{clean}}}$. This is also in accordance with the fact that the lift curve is translated / shifted up-left with flap extension. However, something that was not expected is that the $C_{L_{\alpha_{landing}}}$ coefficient is lower than for the clean condition $C_{L_{\alpha_{clean}}}$. Indeed, the up-left shift of the lift curve resulting from a flap extension is not usually described to be accompanied with modification of slope of the $C_L - \alpha$ curve, and if this is the case it usually results in an increase of the C_{L_α} coefficient and not a decrease.

5.2 Lateral-Directional Model Comparison

In this section lateral-directional aerodynamic models are developed and validated. This is done by the introduction in the pool of model terms candidates such as:

$$\left[\left(\frac{1+\sqrt{X_L}}{2}\right)^2 * \alpha_L - \left(\frac{1+\sqrt{X_R}}{2}\right)^2 * \alpha_R\right], (1-X_L), (1-X_R), (X_R-X_L),$$
$$max((1-X_L),(1-X_R)), min((1-X_L),(1-X_R)), max(0.5,X_L), max(0.5,X_R) \quad (20)$$

representing the effects of individual flow separation component over each wings or the effect due to differential flow separation. To save space, we only present results for the aircraft in clean configuration.

Similarly, as described in section (5.1.2), the X parameters values estimated for either the '2X $2C_{L_\alpha}$' model or the '2X $1C_{L_\alpha}$' model were very close. For this reason, only one set of X parameters was selected concerning the 2X model - in this case, the X parameters values estimated from the '2X $2C_{L_\alpha}$' model were used, as they seemed to be the most accurate and precise ones.

The model term selection algorithm is based on the ranking of the candidate terms according to the effect they have on the PSE (as described in the section 4.4). Considering the candidate terms, as stated before, all the 1st order candidate terms that we want to take into consideration for the building of the model are manually entered. If higher order parameters are desired, they are automatically generated by the algorithm, from cross-products of the original first order terms, up to the desired maximum order.

When the model term selection process is initiated, it computes the possible contribution of the candidate terms to the global aerodynamic model coefficient. If the minimum PSE is reached the algorithm stops. This procedure is done for each training data set and the candidate terms are ranked. Finally, to select which terms will be part of the model, a plot that shows in how many sets each candidate term was selected by the algorithm is created.

On the presented plots a vertical dotted line is present at the place which represents half of the training data sets. This may serve as a coarse metric to include or not a possible candidate term in the final aerodynamic coefficient model.

The procedure is exactly the same for the 1X model or the 2X model. Once both variants of the aerodynamic models are completed and built, they can be compared in their efficiency in modeling the asymmetric dynamics of the aircraft during stalls. Additionally, the 2X model which includes the new differential flow separation terms (depending eventually on ΔX and / or ΔC_{L_α}) can be evaluated.

Concerning the classical model with a unique flow separation point X, after model term selection based on multivariate orthogonal function modelling, it was observed that keeping terms selected in *at least* 75% of the data sets yielded the most accurate models in terms of residual MSE and other statistical indicators. To establish the global model, terms were selected from order 1 and order 2 model selection candidate terms proposal, only keeping the best contributing terms and getting rid of any redundancies in the selected terms.

For the $2X$ model, the same findings were made. Hence, the model terms were selected the same way, except for a small detail that must be noted : to specifically model the aerodynamic coefficients governing the lateral-directional dynamic, terms containing the differential values of the flow separation points (such as $\Delta X = (X_L - X_R)$ or $\Delta C_x = \left[\left(\frac{1+\sqrt{X_L}}{2}\right)^2 * \alpha_L - \left(\frac{1+\sqrt{X_R}}{2}\right)^2 * \alpha_R\right]$) were selected in priority if they were selected in *at least* 50% of the data sets in this case.

5.2.1 Rolling Moment Coefficient (C_l) models

The rolling moment coefficient C_l has a crucial role in the asymmetric dynamics of an aircraft. Thanks to the possibility of having different flow separation points locations on each of the wings, new asymmetrical terms are automatically introduced, depending on X_L and / or X_R, their differential values, etc.

After investigating different maximum desired orders for the model, i.e. by introducing and / or removing certain candidate terms to the pool of regressors different "possible" aerodynamic model of the rolling moment C_l have been developed.

For each of the resulting models, the estimation of its parameters and the computation of statistics to evaluate the model fit quality, accuracy and fidelity, have also been undertaken.

After the model term selection has been done for terms of the 1st and 2nd degree, and after having observed the individual terms contributions to the model, it was concluded that the Rolling Moment can by quite accurately described by equation 21

$$C_l = C_{l_0} + C_{l_{\Delta C_{L\alpha}}} \left[\left(\frac{1+\sqrt{X_L}}{2} \right)^2 \alpha_L - \left(\frac{1+\sqrt{X_R}}{2} \right)^2 \alpha_R \right] + C_{l_\beta}\beta + C_{l_{\delta_a}}\delta_a + C_{l_{\alpha,\Delta X}}\alpha\Delta X \tag{21}$$

Rolling moment coefficient model accompanied by its significant terms with the $2X$ model

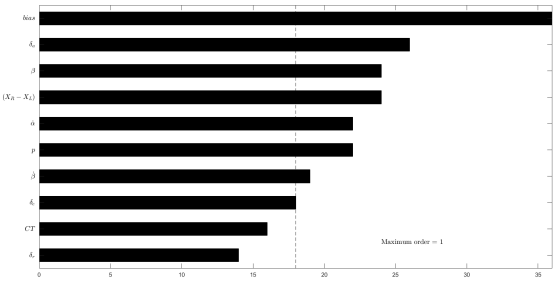

Fig. 9 C_l **model term selection -** $2X$ **| order 1**

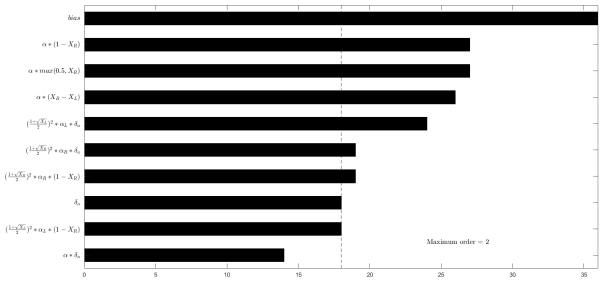

Fig. 10 C_l **model term selection -** $2X$ **| order 2**

The formulation of the model containing a unique flow separation point X at a 75% confidence rate is as follow :

$$C_l = C_{l_0} + C_{l_\beta}\beta + C_{l_{\alpha,\delta a}} \left(\frac{1+\sqrt{X}}{2} \right)^2 \alpha\delta_a + C_{l_{\dot{\alpha}}}\dot{\alpha} \tag{22}$$

Rolling moment coefficient model accompanied by its significant terms considering a unique flow separation point X

One can observe the existence of 'cross-terms', such as $C_{l_{\alpha,\delta a}}$ here, advocating once more the high level of aerodynamic nonlinearities encountered during stall, and the crucial role played by the flow separation point location even if only a unique one is considered. Different metrics to assess model fidelity are presented in table 11.

With $\hat{\theta}$ representing the estimated parameter and $\sigma(\hat{\theta})$ the standard variation of the estimated parameter.

According to the model obtained here for the rolling moment, one can observe that the results seem consistent, considering the closeness of the values from the training and the validation data.
In addition, it can be noticed that both the 1X and the 2X models have similar accuracy. The 2X model seems to be somewhat more accurate, according to the slightly higher value of coefficient of determination (R2) and of the explained variance (VAF) of this model compared to the 1X model. Nevertheless, considering the small values of the estimated parameters and also, more generally the small value and dynamic range of this aerodynamic coefficient, building an accurate dynamic model with these available data is not trivial.

Table 11 Resulting parameters and model accuracy for the rolling moment model

	Terms selection								
	Coefficient	Estimations		Training			Validation		
		$\hat{\theta}$	$\sigma(\hat{\theta})$	MSE rel. (%)	R2	VAF (%)	MSE rel. (%)	R2	VAF (%)
1X model	C_{l_0}	0.0008	0.0015	0.0538	0.25	41.79	0.0503	0.33	39.08
	C_{l_β}	-0.0366	0.0418						
	$C_{l_{\alpha,\delta_a}}$	-0.1867	0.1833						
	$C_{l_{\dot{\alpha}}}$	0.1780	1.1652						
2X model	C_{l_0}	-0.0001	0.0011	0.0560	0.31	43.89	0.0716	0.31	67.88
	$C_{l_{\Delta C_{L_\alpha}}}$	0.0314	0.1167						
	C_{l_β}	-0.0303	0.0310						
	$C_{l_{\delta_a}}$	-0.0569	0.0425						
	$C_{l_{\alpha,\Delta X}}$	0.0940	0.6981						

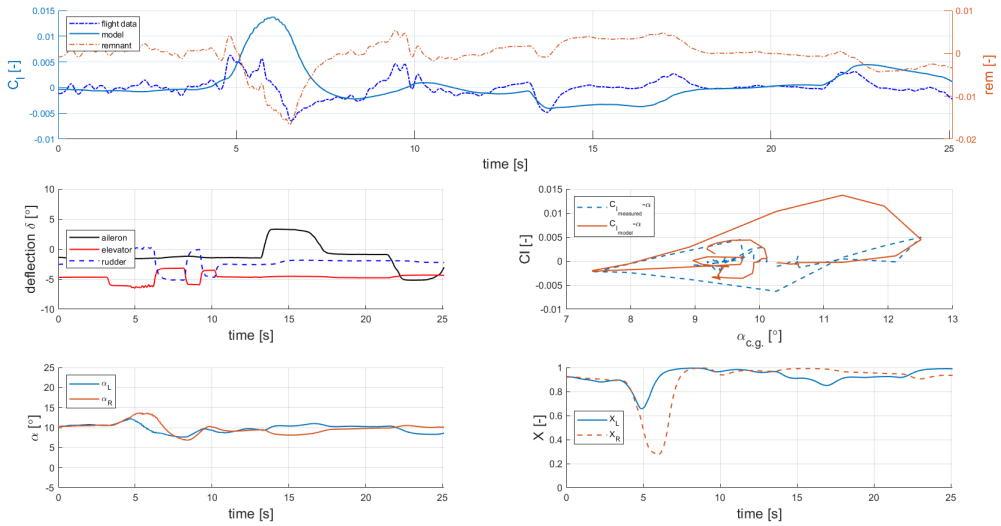

Fig. 11 Example of rolling moment coefficient C_l for the aircraft in clean configuration, during a '3-2-1-1' manoeuvre during the stall

5.2.2 Yawing moment coefficient (C_n) models

The procedure to model the yawing moment coefficient is exactly the same as for modelling the rolling moment. The pool of candidate terms has also been chosen to be the same, because all the necessary terms are already present in this pool of terms.

The level of confidence of the selected terms for the yawing moment coefficient C_n is about the same as the level of confidence of the selected terms for the rolling moment coefficient C_l, with similar thresholds for term selection - once more tuned relatively to the value of the modeled term.

$$C_n = C_{n_0} + C_{n_\beta}\beta + C_{n_{\dot{\alpha}}}\dot{\alpha} \tag{23}$$

Final aerodynamic model chosen for the yawing moment coefficient C_n using the unique X model

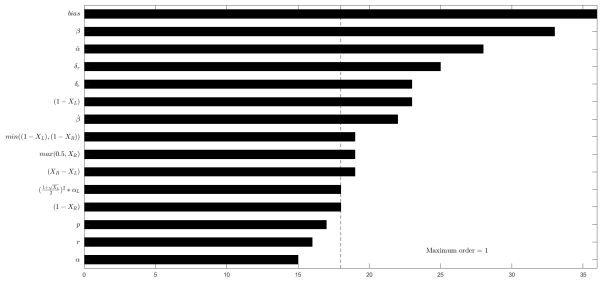

Fig. 12 C_n model term selection - $2X$ | order 1

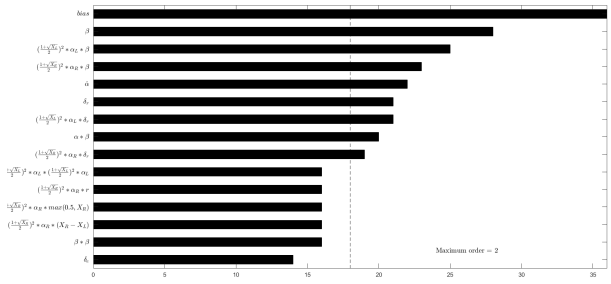

Fig. 13 C_n model term selection - $2X$ | order 2

Considering the 1X model, it consists of terms that do not take into account the flow separation point. Indeed, the only term that could have been integrated in this model, containing X, was $C_{n_{\alpha,\beta}} \left(\frac{1+\sqrt{X}}{2}\right)^2 \alpha.\beta$. But the resulting model, being just as accurate as with the selected $C_{n_\beta}\beta$ term, in order to keep the model parsimonious - which is one of the main goals of this research - the later term was preferred over the more complex former one.
The 2X model is very similar to the 1X model, but with the manually added term due to differential flow separation $C_{n_{\Delta X}}\Delta X$.

$$C_n = C_{n_0} + C_{n_\beta}\beta + C_{n\dot{\alpha}}\dot{\alpha} + C_{n_{\delta_r}}\delta_r + C_{n_{\Delta X}}\Delta X \tag{24}$$

Final aerodynamic model chosen for the yawing moment coefficient C_n using the $2X$ model

The estimated coefficients of the yawing moment model and the model fidelity metrics are available in table 12. These results show that the developed models are consistent with similar values of the model fit metrics for both the training and the validation data. In addition, the 2X model is once again marginally improved by the introduction of the two distinct flow separation points and their differential value.

Table 12 Resulting parameters and model accuracy for the yawing moment model

	Terms selection								
	Coefficient	Estimations		Training			Validation		
		$\hat{\theta}$	$\sigma(\hat{\theta})$	MSE rel. (%)	R2	VAF (%)	MSE rel. (%)	R2	VAF (%)
1X model	C_{n_0}	-0.0021	0.0015	0.0392	0.37	40.04	0.0405	0.32	46.75
	C_{n_β}	0.0512	0.0241						
	$C_{n_{\dot{\alpha}}}$	0.3044	1.1227						
2X model	C_{n_0}	0.0012	0.0028	0.0352	0.52	63.85	0.0387	0.44	54.66
	C_{n_β}	0.0697	0.0283						
	$C_{n_{\dot{\alpha}}}$	-0.1961	0.6772						
	$C_{n_{\delta_r}}$	0.0814	0.0597						
	$C_{n_{\Delta X}}$	-0.0042	0.0388						

5.2.3 Side-Force Coefficient (C_Y) models

The side-force coefficient was also modeled using the same technique and with an identical pool of candidate terms. The selected terms for the side-force coefficient C_Y also have a similar level of confidence as for the other coefficients modeling asymmetrical dynamics (C_l and C_n) with tuned thresholds relatively to the value of the modeled term for an optimal selection.

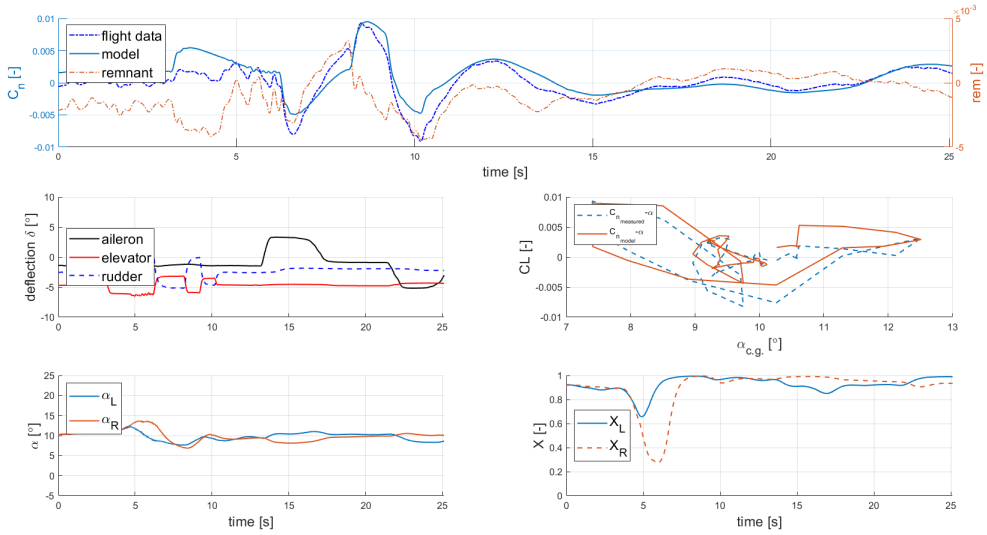

Fig. 14 Example of yawing moment coefficient C_n for the aircraft in clean configuration, during a '3-2-1-1' manoeuvre during the stall

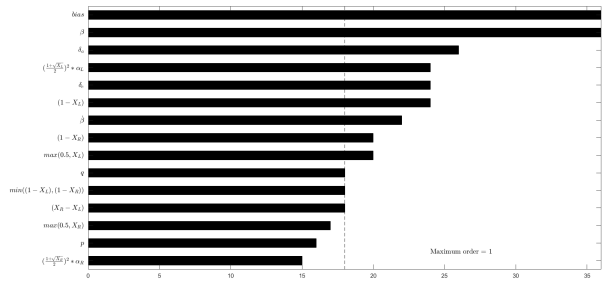

Fig. 15 C_Y model term selection - $2X$ | order 1

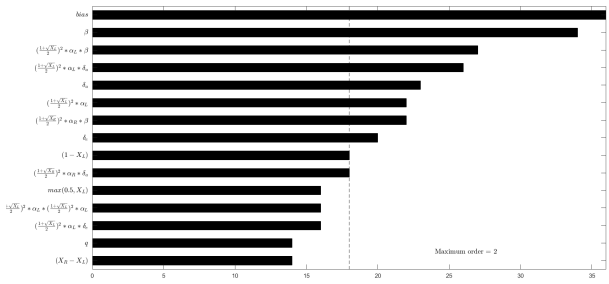

Fig. 16 C_Y model term selection - $2X$ | order 2

The final model formulation for the Side Force coefficient C_Y with the presence of two separate flow separation points is defined in equation 26. For the 1X model, the optimal model structure obtained for the Side Force coefficient C_Y in clean configuration are presented in equation 26. The different estimated model terms and the metrics to estimate the side-force model fidelity are given in table 13.

$$C_Y = C_{Y_0} + C_{Y_\beta}\beta + C_{Y_{\delta_a}}\delta_a + C_{Y_{\Delta X}}\Delta X \tag{25}$$

Final model formulation for the Side Force coefficient C_Y using the $2X$ model

$$C_Y = C_{Y_0} + C_{Y_{\alpha,\beta}}\left(\frac{1+\sqrt{X}}{2}\right)^2 \alpha\beta + C_{Y_{\delta_a}}\delta_a \tag{26}$$

Final model formulation for the Side Force coefficient C_Y using the unique X model

5.2.4 Control surface effectiveness evaluation during stall

For this research work, the focus was on modelling the potential reduction of the effectiveness of the ailerons during stall. In order to try to evaluate the aileron effectiveness reduction during stall, positions of the ailerons and corresponding values of X for which they are completely stalled were computed. In

Table 13 Resulting parameters and model accuracy for the side-force model

	Terms selection								
	Coefficient	Estimations		Training			Validation		
		$\hat{\theta}$	$\sigma(\hat{\theta})$	MSE rel. (%)	R2	VAF (%)	MSE rel. (%)	R2	VAF (%)
1X model	C_{Y_0}	0.0172	0.0094	0.2798	0.49	53.03	0.3174	0.33	65.3
	$C_{Y_{\alpha,\beta}}$	-3.1185	0.8514						
	$C_{Y_{\delta a}}$	-0.0559	0.1336						
2X model	C_{Y_0}	0.0175	0.0096	0.2757	0.53	59.28	0.3141	0.44	82.91
	C_{Y_β}	-0.5228	0.1409						
	$C_{Y_{\delta a}}$	-0.0739	0.1165						
	$C_{Y_{\Delta X}}$	0.0338	0.2334						

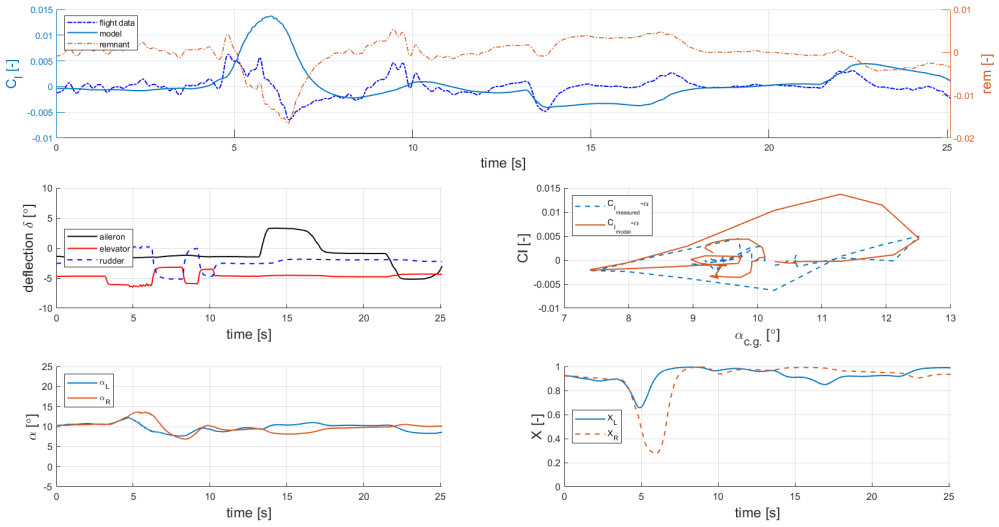

Fig. 17 Example of side-force coefficient C_Y for the aircraft in clean configuration, during a '3-2-1-1' manoeuvre during the stall

Figure 18 on the first subplot, the wings with ailerons are depicted. The dotted grey lines that cross each of the wings are the lines defining $X_{L,R} = 0.5$. They cut the wing in two perfectly equal parts, lengthwise. Additionally, the dotted magenta line is the 'equi-X' line representing the value of X (and thus the wing region) for which the aileron of either the left or the right wing is fully stalled.
This value has been computed, and is equal to $X_{stalled\_aileron} = 0.332$ for the Cessna Citation II aircraft. This plot is designed to provide an animated visual preview of the progression of the flow separation over the wings, other subplots with interesting variables to follow and have a look to are also present on the other subplots. In this case, the second subplot shows the position of the flow separation point over each of the wings separately and the last trio of subplots show other variables such as the considered right wing and left wing angles of attack, the aircraft attitude (roll here), and the aileron input.

Thanks to a specifically developed algorithm that locates in each flight data set the time window during which the flow separation points ($X_{L,R}$) are within a specific range, it was observed that among the training data sets, only very few show the aircraft with both ailerons completely stalled at the same time. However, in a larger number of other data sets the aircraft has at least one of its two ailerons in stalled condition. Nevertheless, the problem is that the duration for which just one of the aileron has

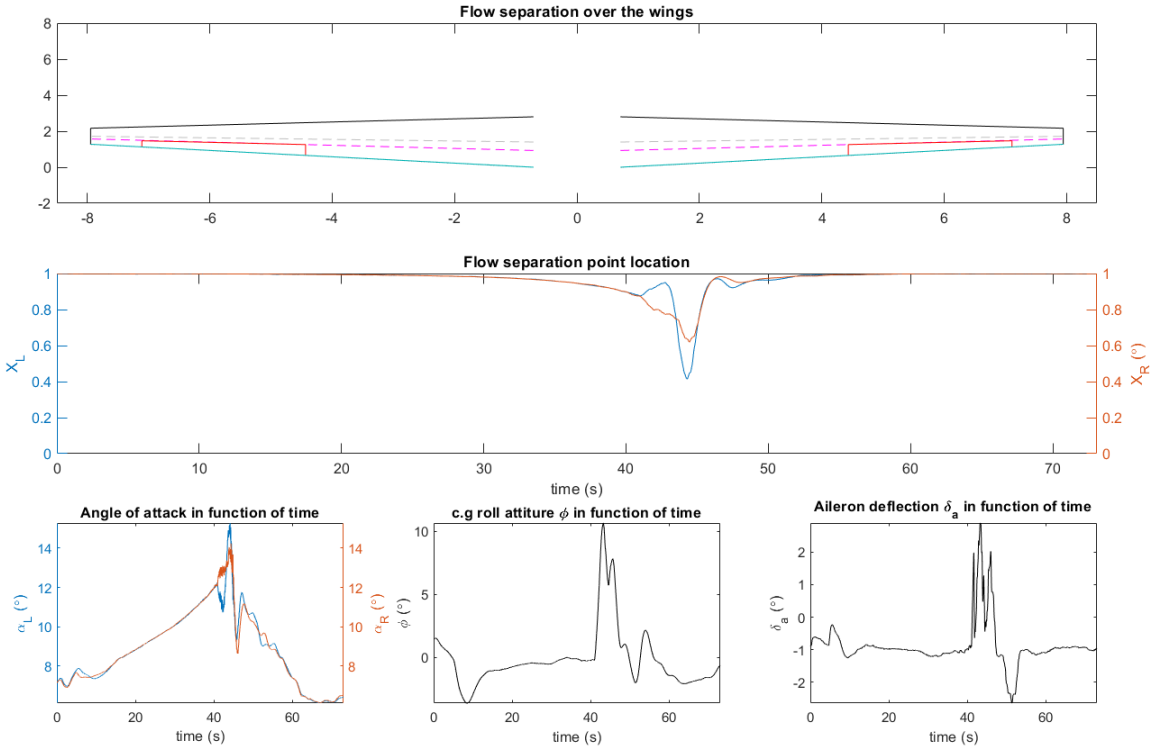

Fig. 18 Plot for flow model progression over the wings, showing ailerons location and corresponding X location for which ailerons are stalled

stalled is short, which reduces the available data volume for modelling this effect. For instance, only 8 aileron stalls in our dataset have a duration of more than 0.5 seconds, and their duration never exceeds 1.31 seconds, which is quite short considering that the mean duration of the stall manoeuvre (3-2-1-1 or control surfaces 'wiggle') performed is about 10 seconds.

An attempt to estimate the aerodynamic parameters ($C_{l_{\delta_a}}$ in particular) during a shorter time window, by windowing the data on a specific part of the manoeuvre (depending on the $X_{L,R}$ values, to ensure ailerons are stalled), was made. However, the results remain inconclusive and working with considerably shorter time windows to estimate parameters substantially reduces estimation accuracy and reliability.
In conclusion, with the available and considered flight test data, no observable and/or notifiable modification or alteration in the control surface effectiveness was observed or detected.

6 Conclusion

The novel modelling approach introducing separate flow separation points X for each wing individually introduces a more versatile and physically meaningful method of modeling aircraft during stalls by allowing the introduction of asymmetric model terms that are each a function of their respective per-wing flow separation variable.
In addition, it opens the door to possible new ways of improving aerodynamic stall models identified from data gathered during stall flight tests. Indeed, flight tests provide measurements on dynamic stall phenomena that currently cannot be obtained through other means, and the proposed modelling approach could exploit the information contained in such datasets.

At this point in time no reduction in modelling performance was found when comparing the new 2X approach to the classical 1X modelling approach. Indeed, the introduction of separate flow separation

points for each wing yields adequate result. A slight improvement in the lateral-directional dynamic model can even be observed to a certain extent which deserves further research.
However, in some cases the optimal aerodynamic model structure, even for the asymmetric aerodynamics, does not contain the flow separation variable X. This by itself indicates that the current flight datasets are not sufficiently informative to robustly estimate aerodynamic model terms that depend on X. Additionally, no significant improvements can be observed with the 2X model when modeling the longitudinal aerodynamics, as Kirchhoff's stall model, which was initially built and used for modeling such dynamics ([4]), was already accurate in this direction as evidenced in part 5.1.

Concerning the lateral-directional aerodynamics, minor yet significant improvements to the model accuracy were provided by the introduction of the two separation point variables. An improvement of 2%-15% was obtained by switching from the 1X to the 2X model. Limited lateral asymmetries are observed in the available flight test data which in turn limits excitation and the ability to estimate related parameters. Hence, an important recommendation for future flight tests is to design maneuvers that are better suited for exciting the lateral asymmetric stall dynamics specifically.

Accurate estimation of control surface effectiveness reduction, and in particular the aileron effectiveness reduction during stall requires more informative data. For this specific input sequences should be designed, possibly automatically, to increase the number of data samples for which at least one of the ailerons is stalled. It should be noted that designing such an input sequence while maintaining adequate safety levels is challenging given that the danger of loss-of-control is present during maneuvers conducted while the aircraft is in a stall.

Finally, this paper presents potential model fidelity improvements as well as the improved flexibility that comes with using two separate flow separation points instead of just one. Flight data in the stall regime is very challenging to obtain, however, as it is not a regime in which an aircraft can spend any significant amount of time. This is particularly true for investigating control surface effectiveness reduction since it requires input sequences that are not aimed at stall recovery but which may in fact deepen the stall. Hence further improving the quality of the models presented in this work may require experiments which cannot be conducted because of safety reasons.

Appendices

6.1 X parameter analysis

This appendix contains details from the nonlinear optimization of the X-parameters.

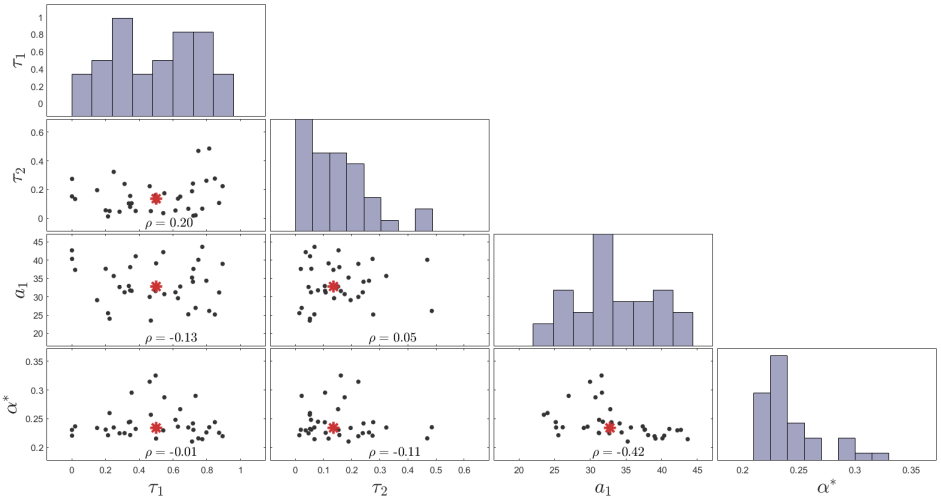

Fig. 19 X parameters dispersion and correlation for the unique flow separation point X model

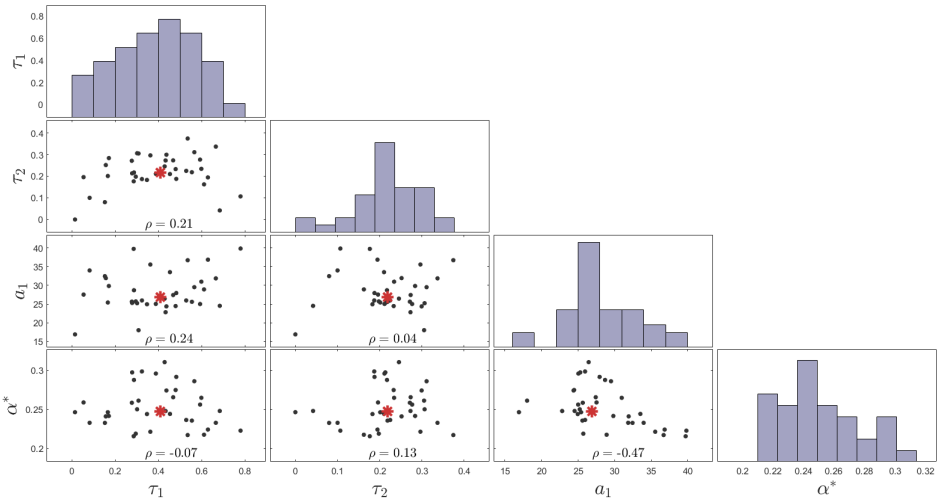

Fig. 20 X parameters dispersion and correlation for the multiple flow separation point $2X$ and $2C_{L_\alpha}$ model

6.2 C_L parameters analysis

These results are obtained after running the linear parameter optimization to estimate C_L parameters considering the - 3 - different possible models, with only one flow separation point or two flow separation point and with or without considering $C_{L_{alpha_L}} = C_{L_{alpha_R}}$

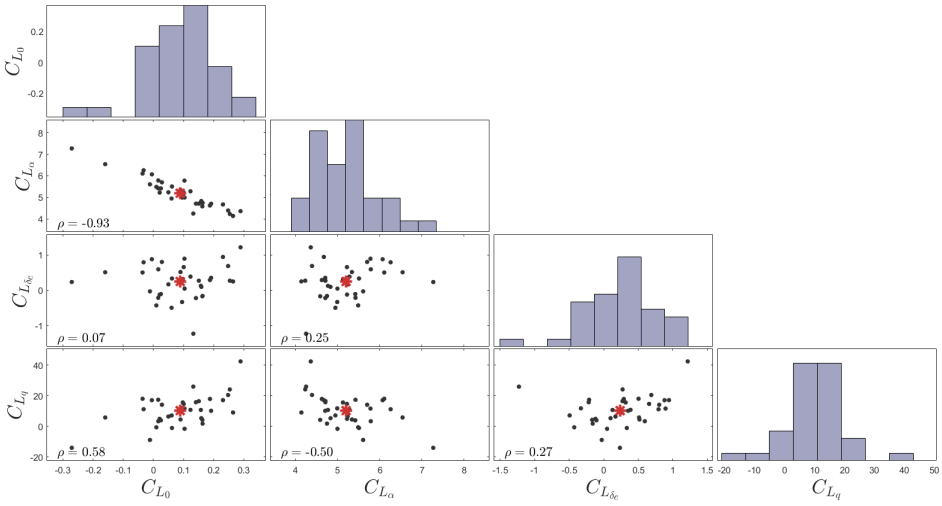

Fig. 21 C_L parameters dispersion and correlation for the $1X$ model

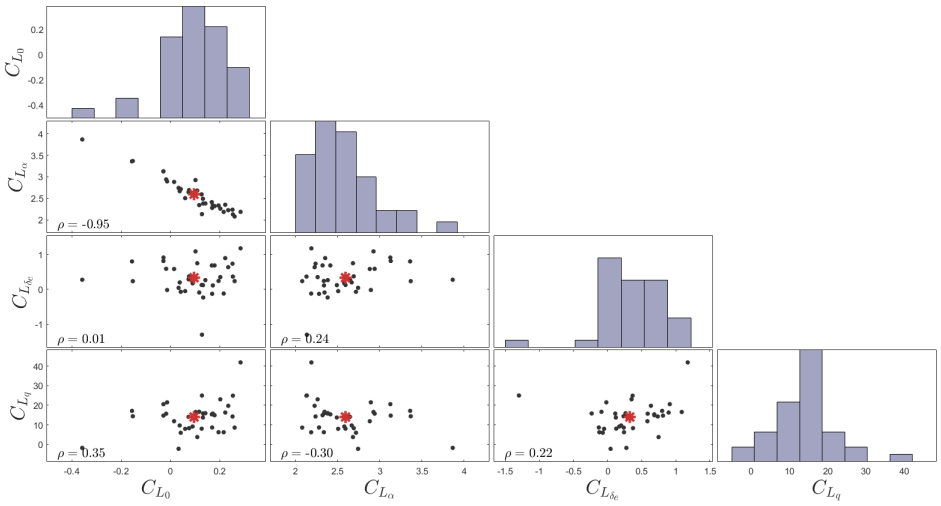

Fig. 22 C_L parameters dispersion and correlation for the $2X$ $2C_{L_{alpha}}$ converted to $2X$ $1C_{L_{alpha}}$ model

6.3 Models of the aircraft in landing configuration

$$\begin{cases} C_{l_{\text{X model}}} = C_{l_0} + C_{l_{\alpha.\delta_a}} \left(\frac{1+\sqrt{X}}{2}\right)^2 \alpha.\delta_a + C_{l_{\alpha.\delta_e}} \left(\frac{1+\sqrt{X}}{2}\right)^2 \alpha.\delta_e + C_{l_{\delta_r}} \delta_r + C_{l_\beta} \beta \\ C_{l_{\text{2X model}}} = C_{l_0} + C_{l_{\delta_a}} \delta_a + C_{l_{\Delta C_{L_\alpha}}} \left[\left(\frac{1+\sqrt{X_L}}{2}\right)^2 \alpha_L - \left(\frac{1+\sqrt{X_R}}{2}\right)^2 \alpha_R \right] + C_{l_{\delta_e}} \delta_e + C_{l_\beta} \beta + C_{l_{\delta_r}} \delta_r \end{cases} \tag{27}$$

Table 14 Resulting parameters and model accuracy for the Rolling Moment coefficient model

	Terms selection								
	Coefficient	Estimations		Training			Validation		
		$\hat{\theta}$	$\sigma(\hat{\theta})$	MSE rel. (%)	R2	VAF (%)	MSE rel. (%)	R2	VAF (%)
1X model	C_{l_0}	0.0064	0.0099	0.1087	0.34	54.65	0.0672	0.38	51.19
	$C_{l_{\alpha.\delta_a}}$	0.4339	0.2494						
	$C_{l_{\alpha.\delta_e}}$	-0.0478	0.1134						
	$C_{l_{\delta_r}}$	0.3304	0.4757						
	C_{l_β}	-0.0352	0.0301						
2X model	C_{l_0}	0.0060	0.0096	0.1087	0.35	45.96	0.0678	0.35	43.16
	$C_{l_{\delta_a}}$	0.0507	0.0362						
	$C_{l_{\Delta C_{L_\alpha}}}$	0.0057	0.0741						
	$C_{l_{\delta_e}}$	-0.0120	0.0168						
	C_{l_β}	-0.0354	0.0306						
	$C_{l_{\delta_r}}$	0.3356	0.4663						

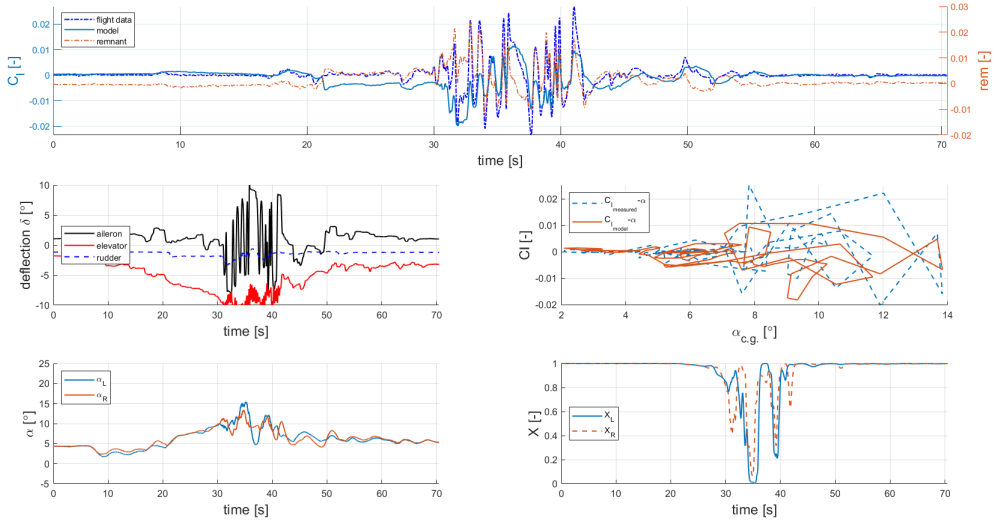

Fig. 23 Example of resulting model for the Rolling moment coefficient with the aircraft in landing configuration.

$$\begin{cases} C_{n_{\text{X model}}} = C_{n_0} + C_{n_\beta} \beta + C_{n_p} p + C_{n_q} q \\ C_{n_{\text{2X model}}} = C_{n_0} + C_{n_\beta} \beta + C_{n_p} p + C_{n_q} q + C_{n_r} r + C_{n_{\Delta X}} \Delta X \end{cases} \tag{28}$$

Table 15 Resulting parameters and model accuracy for the Yawing Moment coefficient model

	Terms selection								
	Coefficient	Estimations		Training			Validation		
		$\hat{\theta}$	$\sigma(\hat{\theta})$	MSE rel. (%)	R2	VAF (%)	MSE rel. (%)	R2	VAF (%)
1X model	C_{n_0}	-0.0007	0.0012	0.0444	0.3	38.45	0.0332	0.48	46.63
	C_{n_β}	0.0494	0.0285						
	C_{n_p}	-0.0026	0.0430						
	C_{n_q}	-0.0948	0.3565						
2X model	C_{n_0}	-0.0007	0.0013	0.0447	0.35	39.6	0.0333	0.5	42.14
	C_{n_β}	0.0525	0.0273						
	C_{n_p}	-0.0117	0.0563						
	C_{n_q}	0.0143	0.4675						
	C_{n_r}	-0.0230	0.0735						
	$C_{n_{\Delta X}}$	0.0011	0.0034						

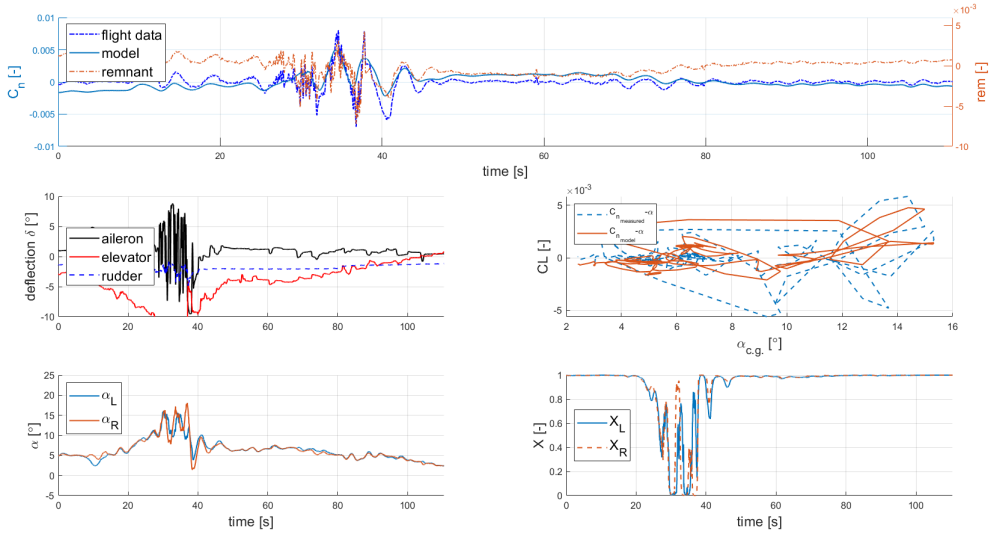

Fig. 24 Example of resulting model for the Yawing moment coefficient with the aircraft in landing configuration.

$$\begin{cases} C_{Y_{\text{X model}}} = C_{Y_0} + C_{Y_\beta}\beta + C_{Y_{\delta_a}}\delta_a + C_{Y_{\alpha.p}}\left(\frac{1+\sqrt{X}}{2}\right)^2 \alpha.p + C_{n_q}q + C_{Y_{\delta_e}}\delta_e + C_{Y_{\delta_r}}\delta_r + C_{Y_{(1-X)}}(1-X) \\ C_{Y_{\text{2X model}}} = C_{Y_0} + C_{n_\beta}\beta + C_{n_p}p + C_{n_q}q + C_{Y_{\delta_a}}\delta_a + C_{Y_{\delta_e}}\delta_e + C_{Y_{\delta_r}}\delta_r + C_{n_{\Delta X}}\Delta X \end{cases} \quad (29)$$

Table 16 Resulting parameters and model accuracy for the Side-Force coefficient model

	Terms selection								
	Coefficient	Estimations		Training			Validation		
		$\hat{\theta}$	$\sigma(\hat{\theta})$	MSE rel. (%)	R2	VAF (%)	MSE rel. (%)	R2	VAF (%)
1X model	C_{Y_0}	0.0130	0.0430	0.4129	0.46	62.22	0.2631	0.39	62.81
	C_{Y_β}	-0.5793	0.2590						
	$C_{Y_{\delta a}}$	0.2590	0.1018						
	$C_{Y_{\alpha.p}}$	-4.2450	3.1179						
	C_{Y_q}	0.5752	2.080						
	$C_{Y_{\delta e}}$	-0.0415	0.1376						
	$C_{Y_{\delta r}}$	0.5760	2.0747						
	$C_{Y_{(1-X)}}$	0.008	1.3390						
2X model	C_{Y_0}	0.01176	0.0422	0.3724	0.4	0.7	0.2710	0.7	60.17
	C_{Y_β}	-0.5578	0.2339						
	C_{Y_p}	-0.4860	0.5180						
	C_{Y_q}	-0.4110	1.6721						
	$C_{Y_{\delta a}}$	0.2616	0.0993						
	$C_{Y_{\delta e}}$	-0.1005	0.1166						
	$C_{Y_{\delta r}}$	0.3770	2.1247						
	$C_{Y_{\Delta X}}$	0.0164	0.1971						

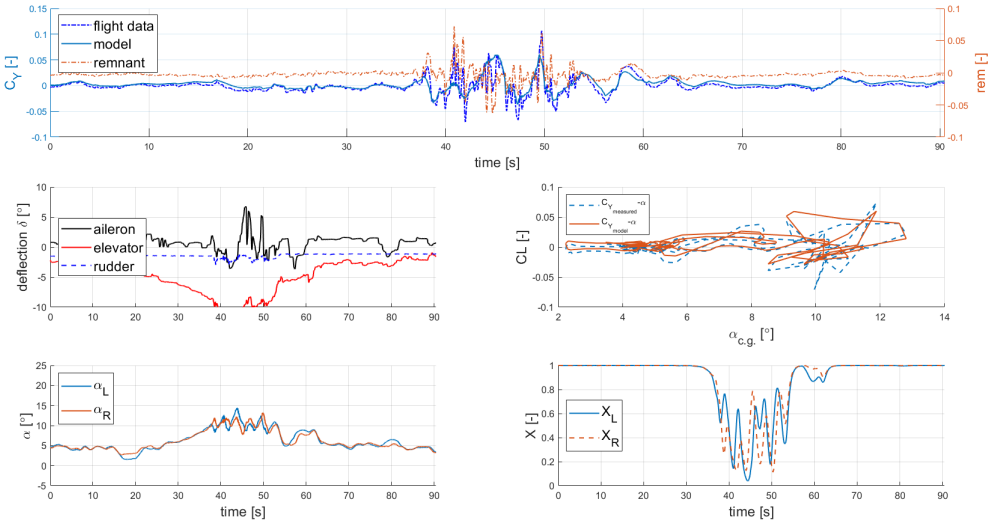

Fig. 25 Example of resulting model for the Side-Force coefficient with the aircraft in landing configuration.

References

[1] ICAO. Accident statistics, 2020. https://www.icao.int/safety/iStars/Pages/Accident-Statistics.aspx.

[2] US Department of Transportation and FAA. Upset prevention and recovery training. *Advisory Circular No: 120-109A*, 2015.

[3] EASA. Certification Specifications for Aeroplane Flight Simulation Training Devices, 2018.

[4] D. Fischenberg. Identification of an unsteady aerodynamic stall model from flight test data. *AIAA 20th Atmospheric Flight Mechanics Conference*, 1995.

[5] D. Fischenberg and R. V. Jategaonkar. Identification of aircraft stall behavior from flight test data. *RTO MP-11*, 1998.

[6] J.B. van Ingen. Dynamic Stall Modeling for the Cessna Citation II. Master's thesis, TU Delft, the Netherlands, 2017.

[7] Laurens van Horssen, Coen C. de Visser, and Daan M. Pool. Aerodynamic stall and buffet modeling for the cessna citation ii based on flight test data. *AIAA Modeling and Simulation Technologies Conference*, 2018.

[8] C. Deiler and T. Kilian. Dynamic aircraft simulation model covering local icing effects. *CEAS Aeronautical Journal, Volume 9, Issue 3, pp. 429–444*, 2018.

[9] Ravindra Jategaonkar. *Flight Vehicle System Identification: A Time Domain Methodology 2nd Ed.* 2015. ISBN: 978-1-62410-278-3. DOI: 10.2514/4.102790.

[10] NLR. Cessna citation ii research aircraft, 2020. https://www.nlr.org/research-infrastructure/research-aircraft.

[11] Multiple Authors. Parameter identification. *NATO AGARD Lecture Series No.104*, 1979.

[12] J.H.Breeman E.Plaetschke, J.A.Mulder. Flight test results of five input signals for aircraft parameter identification. *6th IFAC Symposium on Identification and System Parameter Estimation*, 1982. DOI: https://doi.org/10.1016/S1474-6670(17)63152-5.

[13] J.A. Mulder, J.K. Sridhar, and J.H. Breeman. Identification of dynamic systems - applications to aircraft. part 2: Nonlinear analysis and manoeuvre design. *NATO AGARDograph 300, Flight Test Techniques Series - Volume 3*, 1994.

[14] Sven Marschalk, Peter C. Luteijn, Dirk van Os, Daan M. Pool, and Coen C. de Visser. Stall buffet modeling using swept wing flight test data. *AIAA Scitech 2021 Forum*, 2021. DOI: https://doi.org/10.2514/6.2021-0286.

[15] Jared A. Grauer. Position corrections for airspeed and flow angle measurements on fixed-wing aircraft. *NASA Technical Memorandum*, 2017.

[16] E.A. Morelli. Global nonlinear aerodynamic modeling using multivariate orthogonal functions. *JOURNAL OF AIRCRAFT*, 32(2):270–277, 1995.